Superposition of induced polarization signals measured on pyrite–sand mixtures

Martin, Tina; Weller, Andreas

Published in:
Geophysical Journal International

DOI:
10.1093/gji/ggad091

2023

Document Version:
Publisher's PDF, also known as Version of record

Geophysical Journal International

Geophys. J. Int. (2023) **234,** 699–711
Advance Access publication 2023 March 02
GJI Applied and marine geophysics

https://doi.org/10.1093/gji/ggad091

Superposition of induced polarization signals measured on pyrite–sand mixtures

Tina Martin [1] and Andreas Weller [2]

[1] *Division of Engineering Geology, Lund University, Lund,* 22363*, Sweden. E-mail: tina.martin@tg.lth.se*
[2] *Institute of Geophysics, Clausthal University of Technology, Clausthal-Zellerfeld,* 38678*, Germany*

Accepted 2023 February 21. Received 2022 June 9; in original form 2022 November 8

SUMMARY

Induced polarization (IP) is a common method in ore exploration. IP spectra measured over a wide frequency range can be used to characterize material properties of ores, slags and other residual material from mines and processing facilities. Previous studies have shown that IP parameters are sensitive to type, content or grain size of electronically conductive or semiconductive minerals. Up to now, a variety of experiments has been performed on sand mixtures with fractions of ore minerals. Most experiments consider only a single fraction with a fixed grain size. We continue a series of experiments that have been done with sand–pyrite mixtures. The presented study compares IP spectra recorded for samples either with a single grain radius fraction (E-samples) or with two different grain radii fractions (Z-samples). The spectra are fitted to Pelton models. A Debye decomposition that provides a relaxation time distribution (RTD) is applied to the complex conductivity spectra. The RTD indicates separated maxima only if the ratio of mean grain radii is larger than a factor five. The resolution of the phase spectra and the spectra of imaginary part of conductivity is lower. Even though the volumetric pyrite content is equal in each fraction, the phase spectra and RTD of the Z-samples indicate much higher signals for the pyrite fraction with smaller grain radius. The same observation is made for the chargeability that shows larger values for decreasing grain radii. This finding contradicts existing theories that consider the chargeability as a suitable proxy of the volumetric content of ore minerals. We explain the observed effect by an interaction between neighbouring pyrite particles. The conductivity of the mixtures of the E-samples increases with decreasing grain radius of the pyrite fraction. This effect is attributed to dissolution effects on the surface of the pyrite particles during the sample preparation. We find that the additive superposition of the phase spectra of two E-samples is in good agreement with the measured phase spectra of the Z-samples (measured superposition) containing the two corresponding pyrite fractions. The agreement is slightly worse for the spectra of imaginary part of conductivity, where the measured superposition overestimates the mathematical superposition. The experimental results of our study motivate a further improvement of existing mechanistic models.

Key words: Electrical properties; Hydrogeophysics; Electromagnetic theory.

1 INTRODUCTION

Induced polarization (IP) has proved to be a valuable tool in the exploration of ore deposits. Recent research projects use the IP method to evaluate the metal content in dumps containing the residues of ore processing facilities (Florsch *et al.* 2017; Qi *et al.* 2018; Martin *et al.* 2020).

The success of the IP method is based on its sensitivity to conductive particles. We use in this paper *metallic particles* (MP) as generic term for electronically conductive material that includes ores, metals, graphite and semiconductors as proposed by Revil *et al.* (2015). An induced current flow through material with MP causes measurable polarization effects at the interface between MP and pore fluid. This phenomenon has been studied in many experiments in the laboratory using different types of MP, a varying amount of MP and different particle sizes (e.g. Grissemann 1971; Pelton *et al.* 1978; Mahan *et al.* 1986; Park *et al.* 2013; Placencia-Gómez *et al.* 2013; Hupfer *et al.* 2016; Tartrat *et al.* 2019). The experiments indicate strong polarization effects even for small amounts of MP. Several studies suggest that the volume percentage of MP controls the magnitude of the IP signal (chargeability and maximum phase) whereas the grain size is related to the relaxation time (e.g. Pelton *et al.* 1978; Gurin *et al.* 2015; Revil *et al.* 2015).

On the other hand, mechanistic or conceptual models have been developed to explain the observed effects (e.g. Wong 1979; Revil *et al.* 2015; Bücker *et al.* 2018, 2019). The models are restricted to general assumptions on the material properties and geometry of the conductive particles. The mathematical modelling is based on physical and chemical laws that are formulated together with appropriate boundary conditions. The model of Wong (1979) is based on the full analytical solution of the Nernst–Plank–Poisson equation. The analytical or numerical solutions provide insight into the relationship between material properties and measurable IP signals. However, there exists no universal model that is able to fully explain all observations of the laboratory experiments.

Our study continues a series of experiments on mixtures of sand with ore minerals. The mixtures were investigated by the spectral induced polarization (SIP) method. Hupfer *et al.* (2016) have reported the influence of ore content, grain size and water conductivity on the IP parameters chargeability and time constant. The results show evidence that beside the grain size, the water conductivity exerts a strong effect on the resulting time constant.

Martin *et al.* (2022) investigated the effects of desaturation of sand–pyrite mixtures. They observed a remarkable increase of relaxation time for decreasing water saturation. The proposed conceptual model confirms the significance of the resistivity of the embedding material for the discharge of polarized ore particles.

Up to now, most experiments have considered samples with a single fraction of conductive particles of a fixed grain size. We extend these investigations on samples with two fractions of pyrite grains with different grain radii. The study should reveal whether the contributions of two different grain sizes can be distinguished. The Debye decomposition (e.g. Nordsiek & Weller 2008) and other approaches assume an additive superposition of the contributions that are characterized by different relaxation times. We examine with our experimental data whether an additive superposition of complex conductivity spectra is justified. For this purpose, the spectra of sand–pyrite mixtures with a single grain size and a fixed pyrite content are recorded. In a second step, two measured spectra that have been recorded with different grain size fraction are summed up to generate a mathematical superposition. In another experiment, the mixture of sand with two grain size fractions are prepared. The resulting spectra of the measured superposition are compared with the spectra of the mathematical superposition. The superposition tests are performed on the spectrum of imaginary part of conductivity, the phase spectrum and the relaxation time distribution (RTD) resulting from a Debye decomposition.

2 THEORY

The electrical properties of soils and rocks include both conduction and polarization effects. The two phenomena can be represented by a complex conductivity $\sigma*$ (or complex resistivity $\rho* = 1/\sigma*$). The real (σ') and imaginary (σ'') components represent the ohmic conduction and the polarization charge transport mechanisms, respectively (e.g. Binley & Slater 2020). The complex conductivity of a sample is determined from measurements of the conductivity magnitude $|\sigma|$ and the phase shift φ between the current and voltage signal. The SIP method considers the frequency dependence of the complex conductivity $\sigma*(f)$ or complex resistivity $\rho*(f)$ with f being the frequency in Hz. The spectra of complex conductivity measured over a wide frequency range provide insight into the conduction and polarization phenomena in porous material.

One option of a quantitative interpretation of SIP data is based on fitting phenomenological relaxation models. One of the most widespread models is the Pelton model (Pelton *et al.* 1978; Tarasov & Titov 2013; Weller & Slater 2022):

$$\rho^*(f) = \rho_{\mathrm{P}}\left[1 - m_{\mathrm{P}}\left(1 - \frac{1}{1 + (i2\pi f\tau_{\mathrm{P}})^c}\right)\right] \tag{1}$$

with four fitting parameters: the DC resistivity ρ_{P}, the chargeability m_{P}, the Pelton time constant τ_{P} and the so-called Cole–Cole exponent c. In our study, we use a modified version of the Pelton model:

$$\rho^*(f) = \left\{\left[\rho_0\left(1 - m_P\left(1 - \frac{1}{1 + (i2\pi f\tau_P)^c}\right)\right)\right]^{-1} + i2\pi f\varepsilon\right\}^{-1} \tag{2}$$

to fit the measured spectra. The term $i2\pi f\varepsilon$ (with ε being an additional parameter with the unit of dielectric permittivity) is used to consider the high-frequency dispersion effects (Florsch *et al.* 2014). Once all parameters have been determined by the fitting procedure, we get the corrected spectra by

$$\rho^*_{\mathrm{cor}}(f) = \left\{[\rho^*(f)]^{-1} - i2\pi f\varepsilon\right\}^{-1}. \tag{3}$$

Appendix A demonstrates the application of this correction procedure. The further spectral analysis uses the corrected spectra. It is performed with the original Pelton model in eq. (1) or a modified Pelton model that assumes an additive superposition of two polarization effects with different parameters for chargeability, time constant and Cole–Cole exponent:

$$\rho^*(f) = \rho_P\left[1 - m_1\left(1 - \frac{1}{1 + (i2\pi f\tau_1)^{c_1}}\right) - m_2\left(1 - \frac{1}{1 + (i2\pi f\tau_2)^{c_2}}\right)\right]. \tag{4}$$

The subscript numbers 1 and 2 indicate the affiliation of the parameter. The original Pelton model in eq. (1) is applied for spectra measured on samples with a single grain size fraction. The spectra of samples with two different grain size fractions are preferably fitted to the double Pelton model in eq. (4).

A more general approach of fitting arbitrary IP spectra is the Debye decomposition (e.g. Nordsiek & Weller 2008). This method is used to recover characteristic parameters like DC resistivity, total chargeability and mean relaxation time. With this approach, the frequency-dependent complex electrical resistivity $\rho*(f)$ describes an IP spectrum that can be fitted by a superposition of k Debye terms ($c = 1$)

$$\rho^*(f) = \rho_{\mathrm{DC}}\left(1 - \sum_{j=1}^{k} m_j\left(1 - \frac{1}{1 + i2\pi f\tau_j}\right)\right), \tag{5}$$

with ρ_{DC} being the direct current (DC) resistivity, m_j and τ_j are pairs of partial chargeability and relaxation time of a single Debye model. The function $m_{\mathrm{j}}(\tau_{\mathrm{j}})$ is referred to as RTD. The k chargeability values m_j, which are related to a set of pre-defined relaxation times τ_j, and the value of DC resistivity ρ_{DC} are the result of a fitting procedure as described by Nordsiek & Weller (2008). To reduce the number of parameters, we determine the integrating parameters total chargeability

$$m_t = \sum_{j=1}^{k} m_j, \tag{6}$$

and mean relaxation time

$$\tau_{\text{mean}} = \exp\left(\frac{\sum_{j=1}^{k} m_j \ln(\tau_j)}{m_t}\right). \quad (7)$$

Considering the spectra of resistivity amplitude, the chargeability value can be also approximated by

$$m_a = \frac{\rho(f_{\text{low}}) - \rho(f_{\text{high}})}{\rho(f_{\text{low}})}, \quad (8)$$

with $\rho(f_{\text{low}})$ being the resistivity at the lowest frequency and $\rho(f_{\text{high}})$ the resistivity at the highest frequency (e.g. Seigel 1959).

The origin of the electrical relaxation of charged MP embedded in a porous conducting medium has been discussed for more than five decades (e.g. Wong 1979; Revil *et al.* 2015; Bücker *et al.* 2018, 2019; Gurin *et al.* 2019). Following the approach, which is based on the effective medium theory, the so-called Maxwell–Clausius–Mossotti mixing equation relates the conductivity of the effective complex conductivity σ^* to the conductivity of the background material σ_b^*, the conductivity of the MP σ_{MP}^* and the volume fraction of the MP p_v (e.g. Gurin *et al.* 2015; Revil *et al.* 2015):

$$\frac{\sigma^* - \sigma_b^*}{\sigma^* + 2\sigma_b^*} = p_v \frac{\sigma_{\text{MP}}^* - \sigma_b^*}{\sigma_{\text{MP}}^* + 2\sigma_b^*}. \quad (9)$$

According to the model of Wong (1979), the MP are isolators at low frequencies ($\sigma_{\text{MP}}^*(f = 0) = 0$) and their conductivity becomes infinite at high frequencies ($\sigma_{\text{MP}}^*(f = \infty) = \infty$). Applying eq. (9) with these limits and considering a real background conductivity provide:

$$\sigma_0 = \sigma_b \frac{(1 - p_v)}{\left(1 + \frac{1}{2}p_v\right)} \approx \sigma_b \left(1 - \frac{3}{2}p_v\right), \quad (10)$$

$$\sigma_\infty = \sigma_b \frac{(1 + 2p_v)}{(1 - p_v)} \approx \sigma_b (1 + 3p_v). \quad (11)$$

Using eqs (10) and (11), Gurin *et al.* (2015) propose a formulation for the chargeability m that considers the chargeability of the background material m_b:

$$m = 1 - (1 - m_b)\frac{2(1 - p_v)^2}{(2 + p_v)(1 + 2p_v)}. \quad (12)$$

In absence of background chargeability ($m_b = 0$), a simplified version of eq. (12) predicts a linear relationship between chargeability and the volume fraction of MP (Revil *et al.* 2015):

$$m = \frac{9}{2} p_v. \quad (13)$$

Regarding the effective medium theory with the resulting eqs (12) and (13), the chargeability seems only to depend on the volumetric content of MP. Therefore, the chargeability is regarded as a suitable proxy of p_v. However, various experiments with MP have shown that the chargeability depends additionally on the size of MP (e.g. Grissemann 1971; Pelton *et al.* 1978; Mahan *et al.* 1986; Grissemann *et al.* 2000; Park *et al.* 2013), the type of mineral (e.g. Park *et al.* 2013; Gurin *et al.* 2015; Hupfer *et al.* 2016) and the state of the metallic surfaces (Gurin *et al.* 2019).

In our study, we provide new experimental data to investigate the influence of pyrite particles of different grain radii on the complex conductivity spectra, the RTD and the resulting IP parameters like chargeability and time constants.

Table 1: Overview about the measured samples with a single pyrite grain radius (E-samples) and two different pyrite grain radii (Z- samples): grain radii and pyrite content. As mean grain radius of the E-samples we used the geometric mean of the lowest and largest grain radius. The mean grain radius of the Z-samples is calculated as geometric mean of the mean grain radii of the two fractions.

Sample	First pyrite grain radius (μm)	Second pyrite grain radius (μm)	Mean pyrite grain radius r_{gm} (μm)	Pyrite content p_v (vol.-per cent)
E 01	31–56	–	42	2.75
E 02	56–100	–	75	2.75
E 03	100–177	–	133	2.75
E 04	177–315	–	236	2.75
E 05	315–500	–	397	2.75
E 06	500–1000	–	707	2.75
Z 01	31–56	500–1000	172	5.50
Z 02	56–100	500–1000	230	5.50
Z 03	100–177	500–1000	307	5.50
Z 04	177–315	500–1000	409	5.50
Z 05	315–500	500–1000	530	5.50

3 MATERIAL AND METHODS

3.1 Samples

We investigated eleven unconsolidated pyrite–sand mixtures made of pyrite grains and pure quartz sand. The pyrite grain radius varied for the different samples and was between 31 and 1000 µm while the quartz sand grain radius ranges between 56 and 178µm. We prepared six samples with a single pyrite grain radius mixed with sand (E-samples) and five samples with two different grain radii in the sand (Z-samples). The pyrite mineral content of the mixtures with a single pyrite grain radius was 2.75 vol.- per cent. The mixtures with two pyrite grain radii were composed of 2.75 vol.- per cent of the lower pyrite grain radius fraction and additional 2.75 vol.- per cent of the larger pyrite grain radius resulting in a volume percentage of 5.50 per cent. Table 1 provides an overview about the samples used in the presented study.

The mixture of pyrite and sand material was prepared and packed into the sample holder using always the same recipe (based on the cross-riffling method) to ensure homogenous and reproducible samples as well as comparability between the different samples (see also Hupfer *et al.* 2016; Martin *et al.* 2022). The packing of the material into the sample holder took place stepwise, adding water (0.01 mol L^{-1} NaCl) for each respective step until the sample holder was fully filled. Using this packing procedure, nearly full saturation was achieved. We determined a mean porosity of 39.4 per cent with a maximal variation of 1.5 per cent.

Preliminary tests indicated negligible polarization effects for fully saturated sand samples. The recorded phase shifts did not exceed 0.5 mrad for frequencies below 1 kHz. Therefore, the background chargeability of the sand can be ignored in the interpretation of the experimental results.

3.2 Sample holder and instrument

The unconsolidated samples were measured in a four-point sample holder with a central piece—hosting the sample—and two outer parts on each end for the coupling fluid. The current injection occurred via plate electrodes at the outer parts while tensiometer taps with a porous ceramic were used as potential electrodes right across the sample. The IP spectra of the samples were recorded with the

SIP–ZEL impedance spectrometer in a frequency range between 0.1 Hz and 45 kHz (Zimmermann *et al.* 2008). The sample holder is placed in a climate chamber with a fixed temperature of 20 °C.

The full setup of the measurements and the sample holder design, including a detailed description and figures, can be found in Martin *et al.* (2022) and Hupfer *et al.* (2016).

4 RESULTS

4.1 Complex conductivity spectra

In a first step, we have recorded the IP spectra of all samples. Fig. 1 shows the spectra after removal of the high-frequency effect for the E-samples (single pyrite grain radius) in terms of resistivity ρ (a), phase shift φ (b), real part of conductivity σ' (c) and imaginary part of conductivity σ'' (d). We observe an increase of resistivity amplitude and a decrease of the real part of conductivity with increasing radii of pyrite particles. The phase spectra indicate a decrease of the phase maxima with a shift to lower frequencies for increasing radii of pyrite particles. The imaginary conductivity reveals similar tendencies as the phase.

The corrected IP spectra for the Z-samples (two different pyrite grain radii) are displayed in Fig. 2. While showing the same tendencies as the E-samples in terms of resistivity (a) and real part of conductivity (c), the difference in the maxima of phase shift (b) and imaginary conductivity (d) are lower in comparison to the E-samples. We observe a widening of the spectra of phase and imaginary part of conductivity and a shift of the maximum to higher frequencies for increasing radii difference between the two pyrite grain fractions. Obviously, the difference in grain radii is not sufficient to generate two separated phase maxima. However, the phase spectra of samples Z 01 and Z 02 show an asymmetric hunch at the low-frequency side of the phase maxima that indicates the effect of the pyrite fraction with larger grain radii.

4.2 Parameters of the Pelton model and the Debye decomposition

The spectra of the E- and the Z-samples with symmetric phase spectra (Z 03, Z 04 and Z 05) were fitted to the standard Pelton model (eq. 1). The resulting model parameters and the relative root mean square error (*rrms*) are compiled in Table 2. The values *rrms* < 1 per cent indicate a very good fitting quality.

Regarding increasing pyrite grain radii from sample E 01 to E 06, we observe an increase in ρ_P, a decrease in m_P and a strong increase in τ_P. The exponent c of the Pelton model varies in a narrow range between 0.75 and 0.80. The spectra of samples Z 03, Z 04 and Z 05 are well fitted by the Pelton model, too. Due to the higher pyrite content, the Z-samples indicate higher chargeability values.

The parameters of the double Pelton model (eq. 4) for the Z-samples are displayed in Table 3. Similar to the E-samples, an increase in ρ_P with increasing radii of the fraction of smaller pyrite grains can be seen. The other parameters do not show such a clear trend. The addition of the chargeability values ($m_{P1} + m_{P2}$) as shown in the rightmost column indicates similar values in comparison with the values m_P shown in Table 2 for the Z-samples.

In addition to the Pelton model, a Debye decomposition was performed for all samples. The resulting integrating parameters are compiled in Table 4 together with the chargeability value m_a calculated with eq. (8). In general, a decrease in the chargeability values with increasing pyrite grain radii can be observed. Similar to the time constant τ_P in Table 2, τ_{mean} increases with rising grain radii.

4.3 Superposition of spectra of different grain radii

Fig. 3 illustrates the superposition of spectra belonging to samples with varying grain radii. The left-hand column shows the spectra of the imaginary conductivity σ'', the middle column the phase spectra φ and the right-hand column the RTD resulting from the Debye decomposition.

Each graph displays the spectra of two E-samples (dotted lines in green and blue) together with the measured spectra of the corresponding Z-sample (*measured* superposition shown with red solid lines) that contains the grain radii fractions of the two E-samples. Furthermore, the *mathematical* superposition adds up for each frequency (or relaxation time) the corresponding values of the two E-samples. The spectra of the *mathematical* superposition are displayed as orange solid lines. We select Fig. 3(b) as an example to explain the details of the graph. It displays the phase spectra for the samples E 01 (pyrite grain radius 31–56 μm, green line) and E 06 (pyrite grain radius 500–1000 μm, blue line) together with the measured phase spectrum of sample Z 01 (two pyrite fractions with grain radii of 31–56 and 500–1000 μm, red line). The orange line represents the sum of the phase values from samples E 01 plus E 06, which corresponds to the *mathematical* or additive superposition.

The graphs in Fig. 3 show for most spectra moderate deviations between *measured* and *mathematical* superposition. The superposition works best for the sample Z 05 with two pyrite fractions with similar grain radii (last row). In this case, the validity of a *mathematical* superposition is well confirmed for the phase spectra. A good agreement between the mathematical and measured superposition is observed for the imaginary conductivity and the RTD, too.

An increasing ratio between large and small grain radii of the two pyrite fractions increases the differences between measured and mathematical superposition. For the imaginary part of conductivity, the mathematical superposition underestimates the measured values, whereas the mathematical superposition of the RTD indicates an overestimation. An exception is the maximum of the RTD for sample Z 01, where the measured maximum that is related to the fraction of small pore radii exceeds the value of the mathematical superposition (Fig. 3c).

The graphs in Fig. 3 enable a comparison of the resolution of the spectra and RTD. The RTD indicates the best spectral resolution. The different grain size fractions are well resolved by individual maxima for ratios of grain radii larger than five (see sample Z 03). We observe a lager maximum for the fraction with lower grain radius. The presence of a second fraction with different grain radius is indicated by an asymmetric shape of resulting spectra of phase shift and imaginary part of conductivity. A clear separation with distinct maxima cannot be seen even for ratios of grain radii larger than 15 (sample Z 01).

4.4 Chargeability versus grain size

Fig. 4 displays the values of chargeability according to the different definitions of m_a (eq. 8), m_P (eq. 1) and m_t (eq. 6) versus the geometric mean of the grain radii range r_{gm} (Table 1) for the E-samples, Z-samples and the *mathematical* superposition values from the respective E-samples. For the Z-samples and the mathematical superposition, the horizontal axis is scaled for the smallest

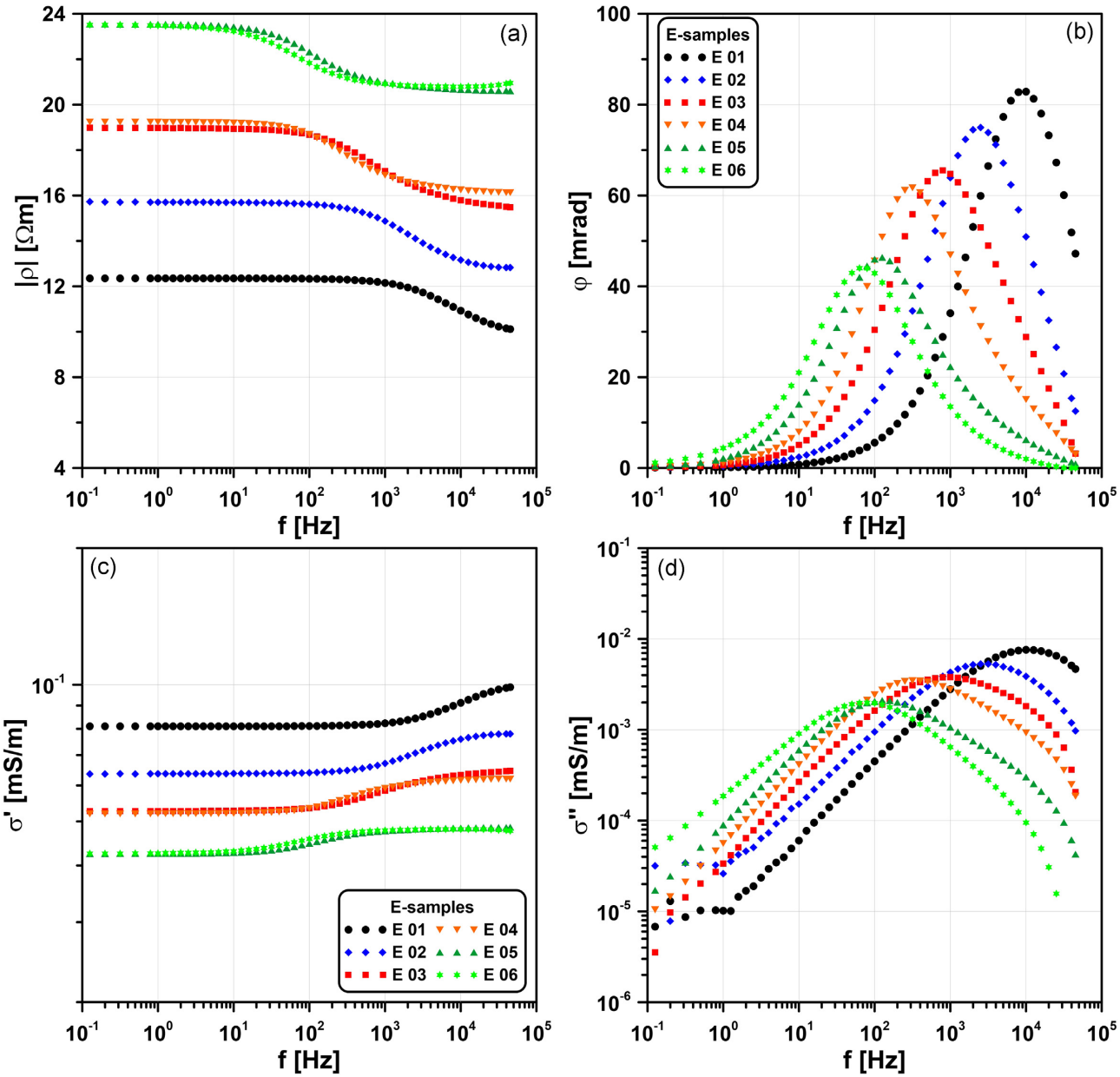

Figure 1. Corrected spectra of the E-samples with a single pyrite grain radius: (a) resistivity amplitude, (b) phase shift, (c) real part of conductivity and (d) imaginary part of conductivity.

grain size fraction (r_{gm_S}). In general, a decrease with increasing grain size can be observed for all chargeabilities. Furthermore, the values of the mathematical superposition overestimate the values determined from the measured spectra of the Z-samples.

4.5 Time constants versus grain size

Fig. 5 shows various time constants as a function of the geometric mean of the grain radii range r_{gm} for the E-samples. The time constants are determined considering the frequency of the maxima in the spectra of σ'', φ, and the imaginary part of complex resistivity ρ'', for example, $\tau_{\sigma''} = 1/\{2\,\pi\,\times f(\max(\sigma''))\}$. Tarasov & Titov (2013) provide the justification for the sequence $\tau_{\rho''} > \tau_{\varphi} > \tau_{\sigma''}$. We observe a continuous increase of all time constants with increasing grain size.

5 DISCUSSION

Our experimental study has confirmed some known qualitative relationships between the parameters that characterize the pyrite sand mixtures and the resulting IP signals. For example, the doubling of the pyrite content in the Z-samples causes higher values of chargeability (Fig. 4). We observed an increase of time constant with increasing grain size (Fig. 5).

Other findings are not in full agreement with published relationships. A variety of studies (e.g. Gurin *et al.* 2015; Revil *et al.* 2015) assumes that the volume content of MP is related in a quantitative way to the parameter chargeability (see eqs 12 and 13). Assuming the validity of these equations, a fixed value of chargeability would be expected for all E-samples because of the constant volumetric content of pyrite particles ($p_v = 2.75$ per cent). A doubling of the pyrite content in the Z-samples ($p_v = 5.5$ per cent) would suggest

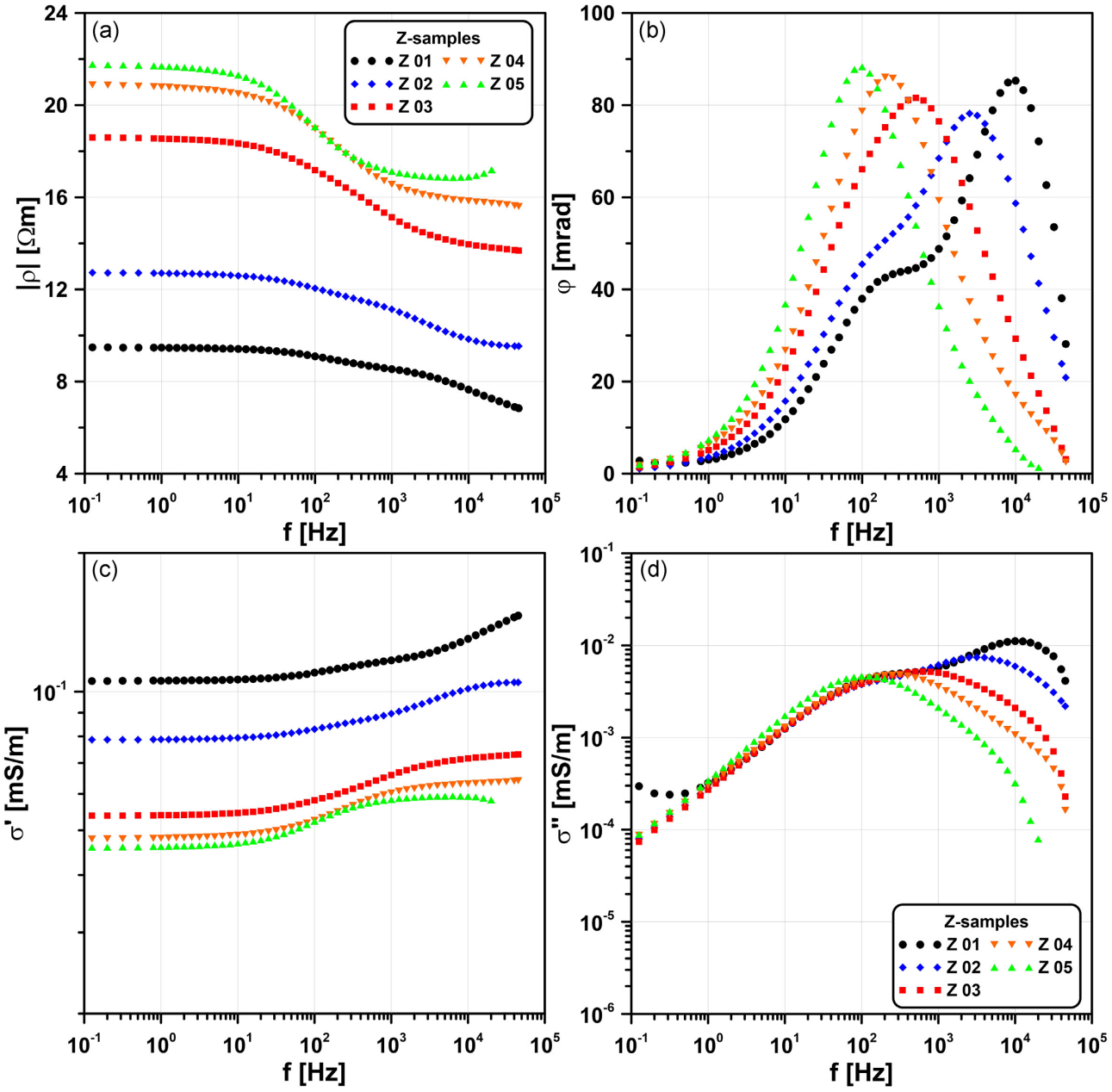

Figure 2. Corrected spectra of Z-samples with two pyrite grain radii: (a) resistivity, (b) phase shift, (c) real part of conductivity and (d) imaginary part of conductivity.

Table 2. Parameters of the Pelton model (eq. 1) for the E- and selected Z-samples.

Sample	ρ_P (Ω·m)	m_P (−)	τ_P (s)	c_P (−)	*rrms* (per cent)
E 01	12.4	0.207	2.10E−05	0.80	0.19
E 02	15.7	0.189	7.60E−05	0.80	0.29
E 03	19.0	0.181	2.10E−04	0.75	0.57
E 04	19.3	0.162	4.90E−04	0.77	0.23
E 05	23.6	0.125	1.30E−03	0.76	0.25
E 06	23.5	0.117	2.40E−03	0.78	0.77
Z 03	18.6	0.266	5.20E−04	0.63	0.41
Z 04	20.8	0.247	9.30E−04	0.70	0.32
Z 05	21.8	0.230	1.90E−03	0.76	0.82

a doubling of the chargeability (eq. 13). In contrary to this expectation, we observe a remarkable dependence of the chargeability on the pyrite grain radii for samples with a constant pyrite content (Table 2 and Fig. 4). Fig. 6 displays the chargeability values from the Pelton model as a function of the mean grain radius. Using eq. (12), a value of $m = 0.116$ is determined for the E-samples (blue horizontal line) and $m = 0.217$ for the Z-samples (orange horizontal line). The samples with the largest grain radii approach the horizontal lines. Obviously, the quantitative relationship formulated in eq. (12) is only valid for MP with grain radii larger than 500 μm.

The effective medium theory ignores the size of the MP. Considering the same volume percentage but different grain radii, the number of MP per volume increases with decreasing grain radii, and consequently the distance between neighbouring particles decreases. Therefore, the interaction of the electrical fields between

Table 3. Parameters of the double Pelton model (eq. 4) for the Z-samples together with the addition of the chargeability values m_P (last column).

Sample	ρ_P (Ω·m)	m_{P1} (−)	τ_{P1} (s)	c_1 (−)	m_{P2} (−)	τ_{P2} (s)	c_2 (−)	$\Sigma\, m_P$ (−)
Z 01	9.47	0.140	1.90E−05	0.94	0.122	7.90E−04	0.68	0.262
Z 02	12.73	0.165	5.50E−05	0.78	0.098	1.60E−03	0.74	0.263
Z 03	18.58	0.158	2.20E−04	0.74	0.102	2.10E−03	0.75	0.260
Z 04	20.84	0.066	5.80E−04	0.69	0.181	1.10E−03	0.71	0.247
Z 05	21.80	0.003	3.40E−04	0.20	0.228	1.90E−03	0.76	0.231

Table 4. Parameters of the Debye decomposition and the approximated chargeability (eq. 8) for E- and Z-samples.

Sample	m_t (−)	τ_{mean} (s)	m_a (−)
E 01	0.202	2.30E−05	0.181
E 02	0.188	8.50E−05	0.184
E 03	0.184	1.90E−04	0.184
E 04	0.163	4.10E−04	0.162
E 05	0.126	1.00E−03	0.125
E 06	0.115	2.60E−03	0.109
Z 01	0.276	9.50E−05	0.279
Z 02	0.259	2.10E−04	0.250
Z 03	0.264	5.30E−04	0.264
Z 04	0.252	9.20E−04	0.253
Z 05	0.225	2.10E−03	0.224

neighbouring MP becomes stronger. We assume that the increase in chargeability magnitude for smaller grain radii may be attributed to the stronger interaction between the MP. This interaction lowers the conductivity at lower frequencies and increases the conductivity at higher frequencies. Considering eq. (8), the chargeability increases. The model of Wong (1979) only considers a single MP in a medium of background conductivity. Therefore, this model is not able to explain the interaction between two particles.

The observed increase of the phase maximum for samples with smaller grain radius (Fig. 1b) contradicts the expectation that the value of the phase maximum can be regarded as a measure of pyrite content (Revil *et al.* 2015). In a similar way, the maximum of the imaginary part of conductivity increases with the decrease in grain radii (Fig. 1d). These observations confirm that neither chargeability nor the maxima of the spectra of phase shift or imaginary part of conductivity provide a direct relationship to the volumetric content of pyrite particles in the sand mixture.

We observe an increasing conductivity level for samples with smaller grain radii (Fig. 1c) that is attributed to an increase of water conductivity after the sample preparation. We saturated all samples with a NaCl-brine of ∼100 mS m^{-1}. However, the chemical reaction of pyrite with water and air during sample preparation causes an increase of fluid conductivity and a decrease in pH shortly after sample preparation as described by Placencia-Gómez *et al.* (2013). Since a monitoring of water conductivity inside the sample holder is impossible, we performed an additional experiment to investigate the temporal change of water conductivity of mixtures of pyrite with water. This experiment confirmed the observations that the largest changes of electrical conductivity of the pore water is observed in the first hours after mixing. Only small changes are observed at times more than 24 hr after sample preparation. Additionally, our experiments confirmed that the largest increase of conductivity is caused by the most fine-grained fraction of pyrite particles. The increase becomes weaker for fractions of larger particles. Other studies tried to compensate the differences in water conductivity by adding fluids of higher salinity (Mahan *et al.* 1986) or by pumping a solution through the sample until a chemical equilibrium is reached (e.g. Gurin *et al.* 2015; Placencia-Gómez *et al.* 2013). Our sample holders did not provide the option to pump fluid through the sample. Therefore, we accepted that the water conductivity (and consequently the sample conductivity) increases with decreasing particle size. We find that the increase of sample conductivity is related to the specific surface area of MP that is inversely proportional to the pyrite grain radius. Previous studies have shown that the chargeability is independent on fluid conductivity (e.g. Gurin *et al.* 2015; Hupfer *et al.* 2016). Therefore, we assume that the changes in fluid conductivity only slightly affect the magnitudes of the phase shift.

Regarding the conceptual model presented in Martin *et al.* (2022), the observed relaxation time depends on both the grain radii of the particle and the resistivity ρ_b of the background material. Considering the effective medium theory, ρ_b is slightly lower than ρ_0. Using eq. (10) and replacing the low frequency resistivity ρ_0 by ρ_P, we get

$$\rho_b = \rho_P \left(1 - \frac{3}{2} p_v\right). \tag{14}$$

The term in brackets of eq. (14) describes a constant factor 0.959 for the E-samples and 0.918 for the Z-samples. Since these factors are close to one, $\rho_b \approx \rho_P$ is a good approximation. As shown in Fig. 1(a) for the E-samples, the resistivity ρ_P increases with rising radii of the pyrite particles. In a similar way, the Z-samples indicate a systematic increase in ρ_P with increasing grain radii of the first pyrite fraction (Fig. 2a). The decrease of ρ_P in the Z-samples in comparison to the higher value in sample E 06 causes a shift of the IP signal of the second pyrite fraction (500–1000 μm) to higher frequencies or lower relaxation time in the RTD. This shift becomes visible in the graphs of Fig. 3. The mathematical superposition considers ρ_b of sample E 06 that is higher than the ρ_b in the Z-samples, which represent the measured superposition. As an example, we refer to the RTD in Fig. 3(c) that indicates a remarkable shift in the position of the left peak that corresponds to the pyrite fraction with the largest grain radius. The mathematical superposition preserves the peak at the position of sample E 06, whereas the measured superposition indicates the peak at a lower relaxation time (consider inverse scaling of the τ-axis). This shift is caused by the lower value of ρ_b in sample Z 01 in comparison with the value in sample E 06. A shift of the signals can be avoided if all experiments are performed with a uniform background resistivity ρ_b.

In order to exclude the influence of ρ_b on the time constant, a correction at a constant value of $\rho_b = \rho_{b-ref}$ is required. We select as reference resistivity the value ρ_P of the sample E 06 (with the largest grain radius) $\rho_{b-ref} = 23.5$ Ω·m. The time constants of the Pelton model are corrected by $\tau_{P-cor} = \frac{\rho_{b-ref}}{\rho_P} \tau_P$. Fig. 7 compares the original and corrected time constants of the Pelton model as a function of the mean grain radius r_{gm}. The power-law fit of the corrected time constants provides an exponent $b = 1.45$. This value is slightly lower than the exponent for the original time constants.

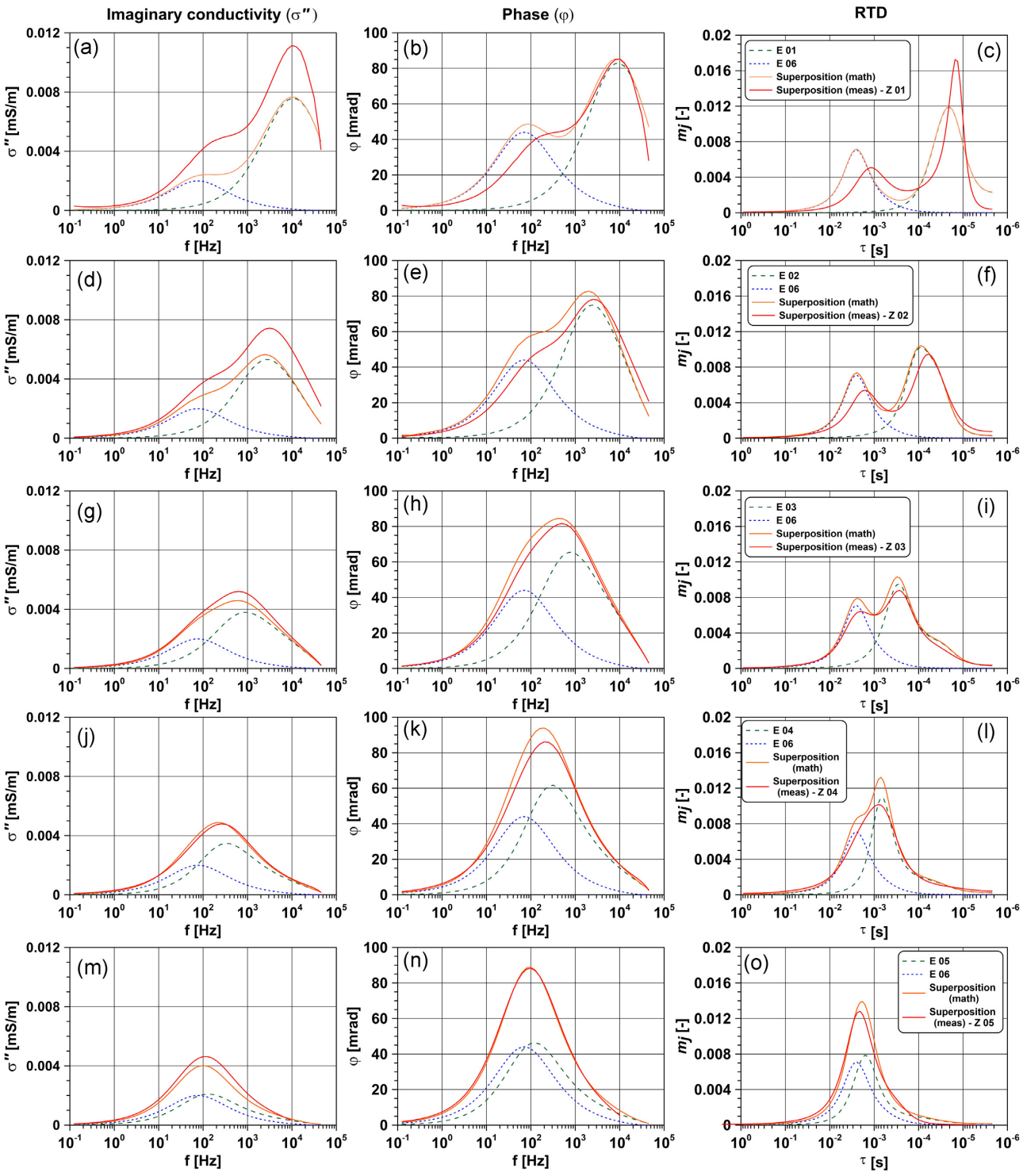

Figure 3. Superposition of spectra of samples with different pyrite grain radii for the imaginary conductivity (σ'', left-hand column), phase shift (φ, middle column) and the RTD from Debye decomposition (right-hand column). Consider that the τ-axis is scaled in inverse direction (from larger to lower values). Therefore, we find in all graphs the indications belonging to the fraction of larger grain radius on the left-hand side.

An exponent b between 1 and 2 is in the expected range of the Wong model (Wong 1979). According to the modelling results of Bücker *et al.* (2018), an exponent $b = 1$ is expected if reaction currents through the solid–liquid interface can be excluded. The presence of electroactive cations in the electrolyte that enable charge transfer reactions causes a quadratic relationship ($b = 2$) between particle radius and relaxation time if the particle radius increases above a critical particle size.

In our experiments, pyrite particles are immersed in a sodium chloride solution. We do not expect any reduction–oxidation reaction on the surface of the pyrite particle. Therefore, another explanation should be found for an exponent $b > 1$. We are aware

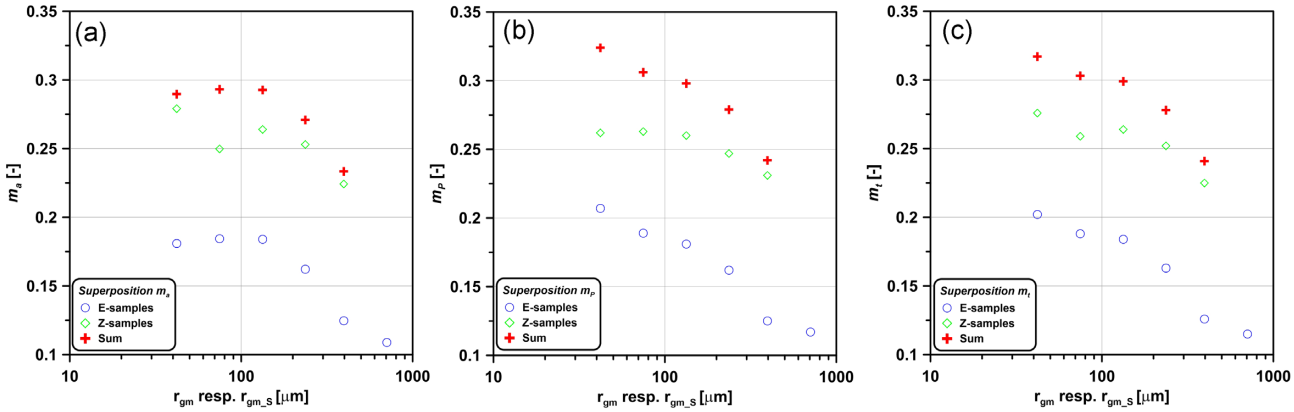

Figure 4. Superposition of different chargeabilities (m_a, m_P and m_t) versus grain size r_{gm} (E-samples) or for the smallest grain size fraction r_{gm_S} (Z-samples). Sum (red crosses) corresponds to the mathematical superposition via addition. (a) Approximate chargeability m_a, (b) chargeability of the Pelton model m_P and (c) total chargeability resulting from the Debye decomposition m_t.

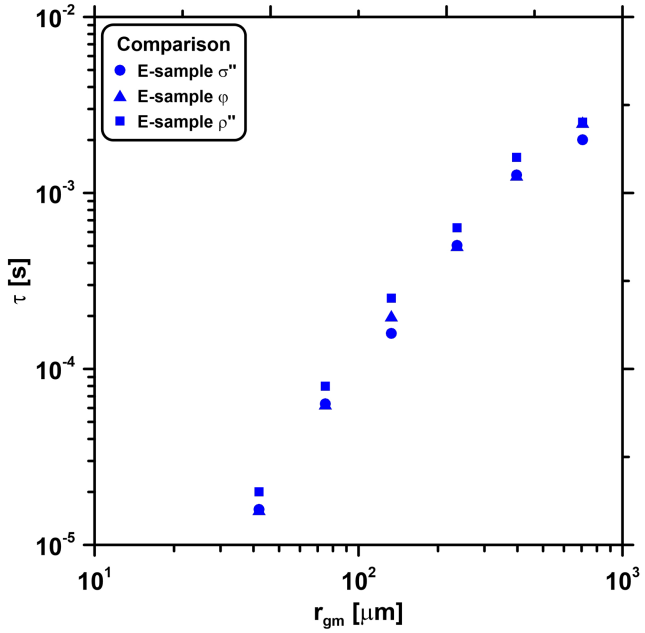

Figure 5. Time constants resulting from different spectra versus grain size r_{gm}.

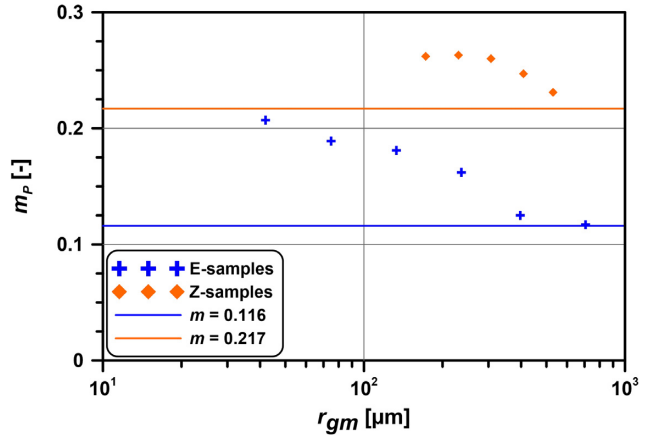

Figure 6. Chargeability from the Pelton model versus grain size for E- and Z-samples. The solid lines are the calculated chargeability values for volumetric pyrite content using eq. (12) (2.75 per cent—blue and 5.5 per cent—orange, respectively).

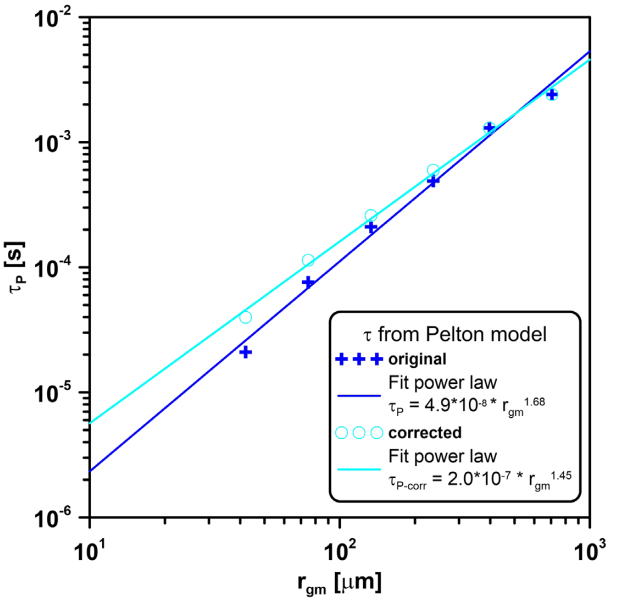

Figure 7. Pelton time constant versus grain size for the E-samples in original (blue crosses) and after correction for the background resistivity (turquoise circles).

that pyrite particles do not fulfill all conditions of the Wong model. Pyrite is a semiconductor that might not be regarded as a perfectly conducting material. On the other hand, the modelling considers ideally spherical particles. The pyrite particle fractions of varying grain size, which were use in our experiments, were generated in grinding and sieving procedures. The crushed particles exhibit irregular shapes and surfaces. We assume that the exponent b is related to the shape and surface topology of the pyrite particles. Further modelling experiments should verify whether rough surfaces with fractal structures would be able to explain exponents $b > 1$.

6 CONCLUSIONS

The comparison of IP spectra measured on sand–pyrite mixtures with both a single grain radius fraction (E-samples) and two grain radii fractions (Z-samples) provides insight in the way the spectra

and the resulting IP parameters can be superimposed. The observations are not in full agreement with models based on the effective medium theory.

Our experiments show clearly that the maxima of phase spectra are decreasing with an increasing grain radius for a fixed volume fraction of pyrite. The same effect is observed for the maxima of the imaginary part of conductivity. Finally, the chargeability, which is an integral parameter that considers the change in conductivity over the measured frequency range, depends on the grain radius, too. This dependence cannot be ignored. For samples with a constant volumetric pyrite content of 2.75 per cent, an increase in mean grain radius from 42 to 707 μm results in a decrease in chargeability m_P from 0.207 to 0.117. We conclude that the interaction between the smaller pyrite particles that are located in close distance to each other cause an increase of chargeability. This effect has consequences for the RTD. The amplitude m_j, which is the partial chargeability of a predefined relaxation time τ_j, does not reflect the volume percentage of a certain grain radius. Although the volume percentage of the two grain radii fraction is equivalent, we observe larger maxima in the RTD for the pyrite fraction with lower grain radii. Therefore, the chargeability cannot longer be regarded as an IP quantity that is the best proxy for the volumetric metal content.

The chargeability resulting from a sand mixture with two grain radii fractions is lower than the mathematical addition of the chargeability values of the two single grain size mixtures. This difference becomes most clear if fractions with a large grain size ratio are regarded. This observation confirms that the chargeability is not an IP parameter that can be simply summed up for all constituents. This conclusion can be extended to the RTD. We observe for most mixtures that the mathematical (additive) superposition of the measured RTD of mixtures with a single grain radius fraction overestimates the partial chargeabilities of the RTD resulting from the measured IP spectra on the mixture with two grain radii fractions. However, the mathematical superposition can be regarded as a useful approximation. The agreement with the measured superposition improves if pyrite fractions with similar grain radii are regarded. The mathematical superposition of phase spectra provides a promising agreement with the measured spectra of the Z-samples. For the spectra of imaginary conductivity, the mathematical superposition underestimates the measured spectra of samples with two grain radii fractions.

We observed an increasing conductivity of the mixtures with decreasing grain radius of the pyrite fraction. This effect is attributed to chemical reactions on the surface of the pyrite particles that cause an increase in fluid conductivity shortly after sample preparation. The change in background conductivity affects the position of the IP signals in the RTD and spectra.

The experimental results of our study provide motivation for a further development of mechanistic models that should include the interaction of electrical fields between neighbouring MP.

ACKNOWLEDGMENTS

Part of this work (laboratory measurements) was done within the master thesis of Laura Behling (Free University of Berlin). Her thesis work was part of the ROBEHA project, which was funded by the German Ministry of Education and Research (grant 033R105). All experiments were conducted in the laboratories at the Federal Institute for Geosciences and Resources (BGR), Germany. We hereby acknowledge the help from Laura Behling, the BGR ground geophysics team and Kerstin Kuhn (also BGR). We thank Thomas Günther (LIAG) for his support with the data processing. AW acknowledges the support of DFG trough grant no. 425975038.

DATA AVAILABILITY

The data underlying this paper will be shared on reasonable request by the corresponding author.

REFERENCES

Binley, A. & Slater, L., 2020. *Resistivity and Induced Polarization – Theory and Application to the Near-Surface Earth*. Cambridge University Press.

Bücker, M., Flores Orozco, A. & Kemna, A., 2018. Electro-chemical polarization around metallic particles – Part 1: the role of diffuse-layer and volume-diffusion relaxation, *Geophysics,* **83**(4), E203–E217.

Bücker, M., Undorf, S., Flores Orozco, A. & Kemna, A., 2019. Electrochemical polarization around metallic particles—Part 2: the role of diffuse surface charge, *Geophysics,* **84**(2), E57–E73.

Florsch, N., Feras, A., Bonnenfant, J. & Camerlynck, C., 2017. La polarisation provoquée, outil géophysique de spatialisation des amas de scories pour lestimation des productions sidérurgiques -induced polarization: a geophysical tool for slag characterization and ancient iron production assessment, *ArcheoScience,* **41-2,** 23–33.

Florsch, N., Revil, A. & Camerlynck, C., 2014. Inversion of generalized relaxation time distributions with optimized damping parameter, *J. appl. Geophys.,* **109,** 119–132.

Grissemann, C., 1971. *Examination of the Frequency-Dependent Conductivity of Ore containing Rock on Artificial Models: Scientific Report No. 2,* Electronics Laboratory, University of Innsbruck, Austria.

Grissemann, C., Rammlmair, D., Siegwart, C. & Fouillet, N., 2000. Spectral induced polarization linked to image analyses: a new approach, in: Rammlmair, D., Mederer, J., Oberthür, T, Heimann, R. & Pentinghaus, H.(eds) *Applied Mineralogy, Balkema,* pp. 561–564, Rotterdam.

Gurin, G., Titov, K., Ilyin, Y. & Tarasov, A., 2015. Induced polarization of disseminated electronically conductive minerals: a semi-empirical model, *Geophys. J. Int.,* **200**(3), 1555–1565.

Gurin, G., Titov, K. & Ilyin, Y., 2019. Induced polarization of rocks containing metallic particles: evidence of passivation effect, *Geophys. Res. Lett.,* **46,** 670–677.

Hupfer, S., Martin, T., Weller, A., Kuhn, K., Günther, T., Djotsa, V. & Noell, U., 2016. Polarization effects of unconsolidated sulphide-sand-mixtures, *J. appl. Geophys.,* **135,** 456–465.

Mahan, M. K., Redman, J. D. & Strangway, D. W., 1986. Complex resistivity of synthetic sulfide bearing rocks, *Geophys. Prospect.,* **34,** 743–768.

Martin, T., Kuhn, K., Günther, T. & Kniess, R., 2020. Geophysical exploration of a historical stamp mill dump for the volume estimation of valuable residues, *J. Environ. Eng. Geophys.,* **25,** 275–286.

Martin, T., Weller, A. & Behling, L. 2022. Desaturation effects of pyrite–sand mixtures on induced polarization signals, *Geophys. J. Int.,* **228,** 275–290.

Nordsiek, S. & Weller, A., 2008. A new approach to fitting induced-polarization spectra, *Geophysics,* **73**(6), 235–245.

Park, M. K., Park, S., Takakura, S., Yi, M.-J. & Kim, J.-H., 2013. SIP response of sulfide minerals in artificial specimen, in *Proceedings of the 11th SEGJ International Symposium,* pp. 407–410, doi:10.1190/SEGJ112013-103 .

Pelton, W.H., Ward, S.H., Hallof, P.G., Sill, W.R. & Nelson, P.H., 1978. Mineral discrimination and removal of inductive coupling with multifrequency IP, *Geophysics,* **43,** 588–609.

Placencia-Gómez, E., Slater, L., Ntarlagiannis, D. & Binley, A., 2013. Laboratory SIP signatures associated with oxidation of disseminated metal sulfides, *J. Contam. Hydrol.,* **148,** 25–38.

Qi, Y., Ahmed, A.S., Revil, A., Ghorbani, A., Abdulsamad, F., Florsch, N. & Bonnenfant, J., 2018. Induced polarization response of porous media with metallic particles part 7: detection and quantification of buried slag heaps, *Geophysics,* **83,** E277–E291.

Revil, A., Florsch, N. & Mao, D., 2015. Induced polarization response of porous media with metallic particles—Part 1: a theory for disseminated semiconductors, *Geophysics,* **80**(5), D525–D538.

Rücker, C., Günther, T. & Wagner, F.M., 2017. pyGIMLi: an open-source library for modelling and inversion in geophysics, *Comput. Geosci.,* **109,** 106–123.

Seigel, H. O., 1959. Mathematical formulation and type curves for induced polarization, *Geophysics,* **24,** 547–565.

Tarasov, A. & Titov, K., 2013. On the use of the Cole–Cole equations in spectral induced polarization, *Geophys. J. Int.,* **195**(1), 352–356.

Tartrat, T. *et al.* 2019. Induced polarization response of porous media with metallic particles—part 10: influence of desiccation, *Geophysics,* **84**(5), E357–E375.

Weller, A. & Slater, L., 2022. Ambiguity in induced polarization time constants and the advantage of the Pelton model, *Geophysics,* **87**(6), E393–E399.

Wong, J., 1979, An electrochemical model of the induced-polarization phenomenon in disseminated sulfide ores, *Geophysics,* **44,** 1245–1265.

Zimmermann, E., Kemna, A., Berwix, J., Glaas, W., Münch, H. & Huisman, J., 2008. A high-accuracy impedance spectrometer for measuring sediments with low polarizability, *Meas. Sci. Technol.,* **19,** 105603.

APPENDIX A: CORRECTION OF HIGH-FREQUENCY DISPERSION EFFECTS

All measured complex resistivity spectra have been fitted by eq. (2) using the function *SIP.removeEpsilonEffect* of the open-source software pyGIMLi (Rücker *et al.* 2017). Once all parameters have been determined, eq. (3) is applied to get the corrected spectra by removing the high-frequency dispersion effects. We demonstrate the results of this procedure for two samples in Figs A1 and A2.

The measured phase spectrum of sample E 06 indicates a strong increase for frequencies larger than 7 kHz (Fig. A1b) that might be caused by electromagnetic coupling effects. The application of the correction procedure results in a bell-shaped phase spectrum that can be well fitted by the original Pelton model (eq. 1).

The application of the correction procedure to sample Z 02 causes a moderate decrease of the phase values in the high-frequency range (see Fig. A2b). The frequency and the magnitude of the phase maximum are only slightly affected by the correction procedure. The corrected spectrum can be well fitted by the double Pelton model in eq. (4).

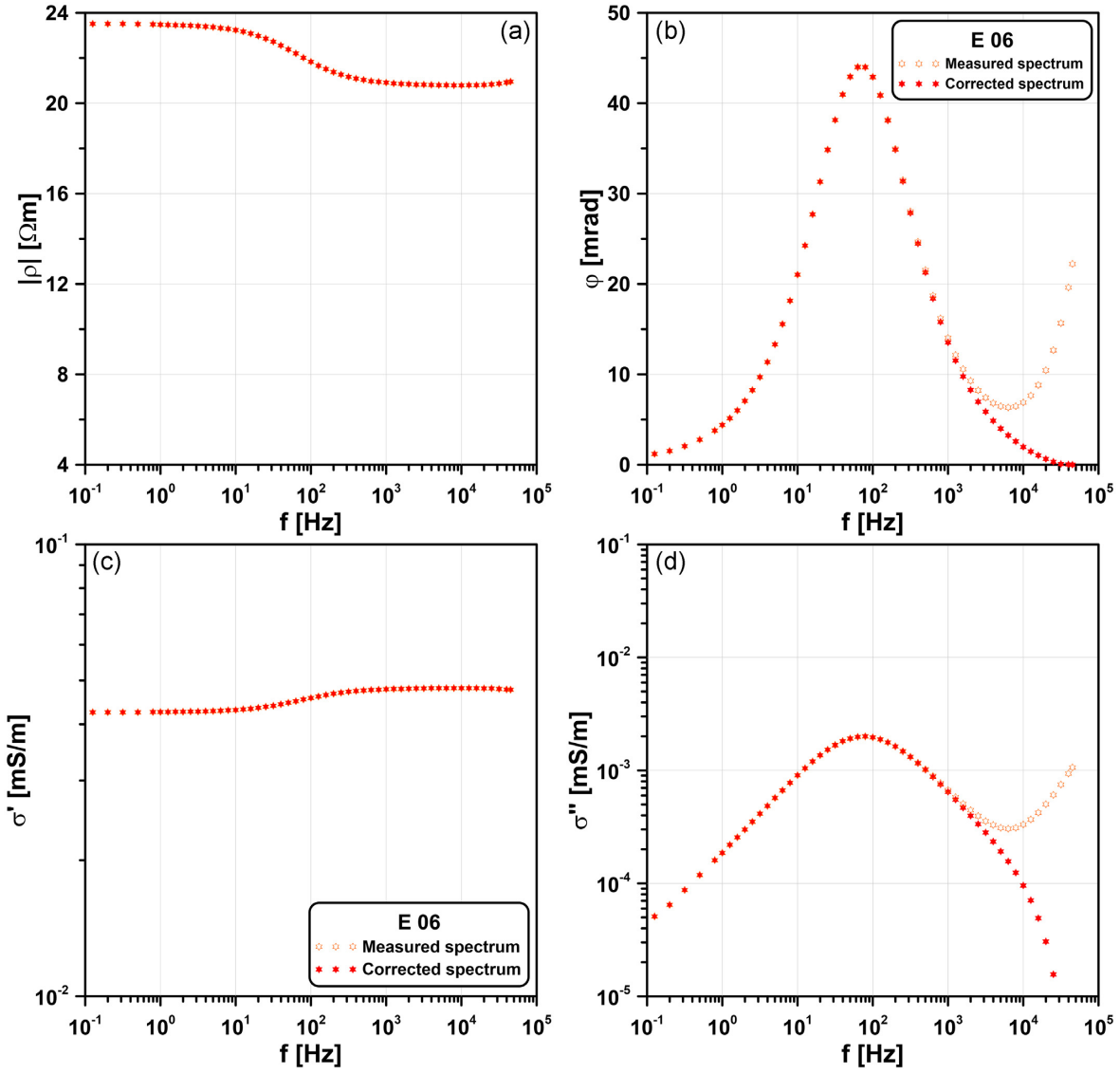

Figure A1. Comparison between original SIP data and spectra after removing high-frequency dispersion effects for sample E 06.

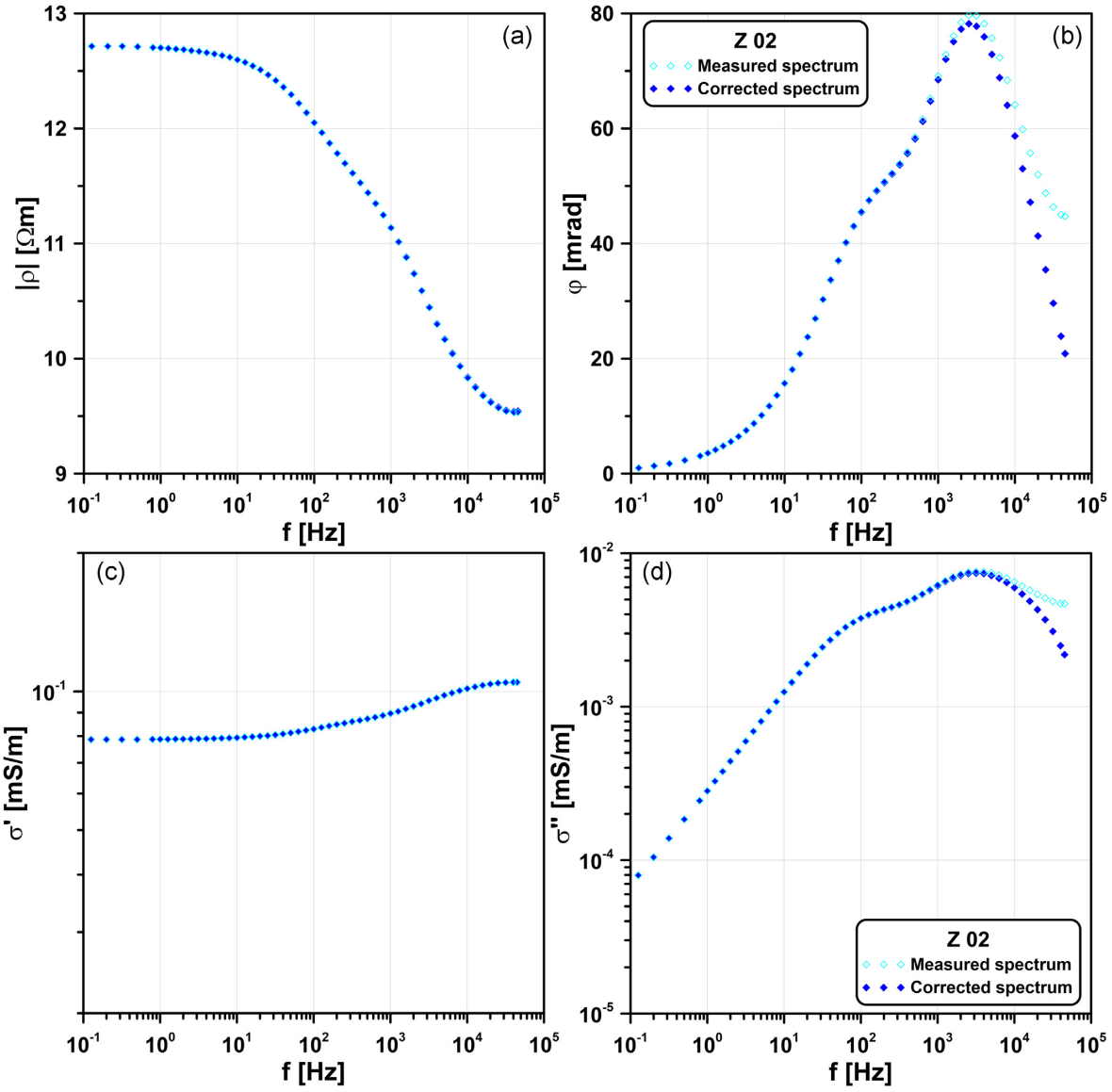

Figure A2. Comparison between original SIP data and spectra after removing high-frequency dispersion effects for sample Z 02.